Remagnetization mechanism and a new age model for L9 in Chinese loess

Chunsheng Jin, Qingsong Liu *

State Key Laboratory of Lithospheric Evolution, Institute of Geology and Geophysics, Chinese Academy of Sciences, Beijing 100029, PR China

A B S T R A C T

Chinese loess during the Quaternary is important for both paleomagnetic and paleoclimatic studies. Although magnetostratigraphy has been used for the initial loess timescale, paleomagnetic records in loess still remain in debates, such as magnetic polarity anomalies in L9, which is a thick and coarse sandy horizon as a typical marker bed. To better understand the magnetization mechanism of these anomalies, a new age model for L9 was first constructed based on a new correlation between loess and marine δ^{18}O, which proposed that L9 should be correlated to marine oxygen stage (MIS) 20–24, not 22–24 as previous suggested. Using combined grain size and environmental magnetism parameters, an extended climatic optimum corresponding to MIS 21 can be identified in middle of L9. A remagnetization mechanism of viscous remanent magnetization overprinting on characteristic remanent magnetization (ChRM) carriers (mainly large pseudo single domain and multidomain magnetite particles), associated with the chaotic detrital remanent magnetization caused by low efficiency alignment of ChRM carriers along with the ambient field during deposition, is proposed to interpret the magnetic anomalies. This study provides new insights into the magnetization mechanism of the Chinese loess, and the new age model for L9 helps to accurately refine the finer scale correlation of paleoclimatic records between the Chinese loess and marine sediments.

© 2011 Elsevier B.V. All rights reserved.

1. Introduction

The wind-blown dust deposited in the northwest of China constitutes one of the most continuous terrestrial loess-paleosol sequences (Liu, 1985), and can be traced backward to the past 2.8 Ma according to the latest results of Yang and Ding (2010). The dust, which was derived mainly from Gobi (stony desert) in southern Mongolia and the adjacent areas (Sun, 2002), began to accumulate in response to the major uplift of the Tibetan Plateau and the evolution of polar ice-sheets, and the associated evolution of Asian atmospheric circulation patterns (Ding et al., 1995; Liu and Ding, 1998; An et al., 2001; Guo et al., 2002b, 2009; Sun et al., 2010a).

The loess deposits (with an area of ~4.4 × 10⁵ km²) are distributed mainly in the Chinese Loess Plateau (CLP) (Fig. 1). All together, there are 34 paleosol horizons (S0–S33, by the pedostratigraphic nomenclature of Liu (1985)) formed during the interglacials, interbedded by 34 loess horizons (L1–L34) formed during the glacial periods (Liu, 1985; Yang and Ding, 2010). As an excellent archive, the Chinese loess preserves detailed records of both paleomagnetic (e.g., Heller and Liu, 1982; Heller and Evans, 1995) and paleoclimatic signals (e.g., An et al., 2001; Ding et al., 2002; Guo et al., 2002b; Sun and Zhu, 2010).

The first order chronological framework was constructed based mainly on the magnetostratigraphy. However, there remains long-standing debate on the acquisition mechanism of the natural remanent magnetization (NRM) for the sandwich layers L8–S8–L9. First, the units L8, S8, and L9 have been traditionally correlated to the marine oxygen isotope stage (MIS) 20, 21, and 22–24, respectively (Heller and Liu, 1984; Kukla, 1987). This strategy was then accepted widely (e.g., Chen et al., 1991; Forster and Heller, 1994; Heller and Evans, 1995; Liu et al., 1999; Heslop et al., 2000; Sun and Liu, 2000b; Porter, 2001; Ding et al., 2002; Sun, 2005; Deng et al., 2006; Sun et al., 2006). However, this correlation yields potential ambiguities. For example, a large lock-in depth of the NRM has been proposed for the last paleomagnetic polarity reversal, the Matuyama–Brunhes (MB) reversal (~780 ka B.P.; Shackleton et al., 1990), between loess and marine sediments (Forster and Heller, 1994; Heller and Evans, 1995). The MB boundary (MBB) was generally located in the loess horizon L8 (a glacial period) in Chinese loess (e.g., Liu et al., 1988a; Rutter et al., 1991; Zheng et al., 1992; Sun et al., 1998; Pan et al., 2002; Yang et al., 2004) and in MIS 19 (an interglacial period) in marine sediments (e.g., Tauxe et al., 1996, and references therein). Recently, Liu et al. (2008) suggested that an inaccurate climatic boundary between L8 and S8 is the main cause for such a confusion of the MBB in loess. They revealed that the MBB was actually located in the upper part of S8, which is consistent with the studies of Heller and Liu (1982), Wang et al. (2005, 2006), and Jin and Liu (2010). Therefore, the
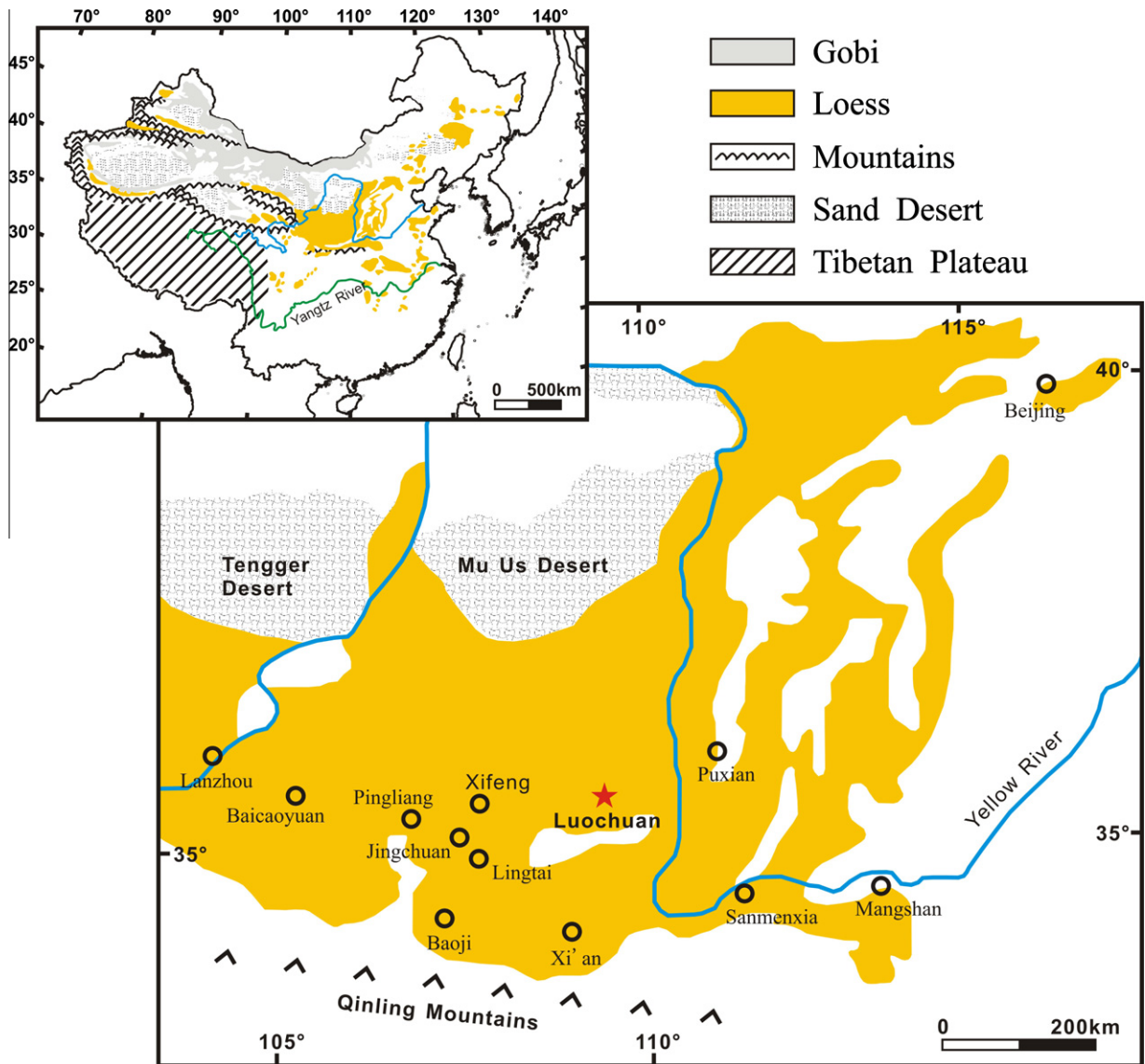
Fig. 1. A schematic map of the distribution of the Chinese loess and the location of the Luochuan section (star). Circles represent the other sections described in the text.

paleosol unit S8 should be correlated to MIS 19 (Wang et al., 2006; Liu et al., 2008; Jin and Liu, 2010). Thus the age model for the loess unit L9 should be adjusted accordingly.

Second, for part of the loess unit L9, the NRM has been remagnetized. Distinct polarity anomalies have been widely detected in L9 in many areas of the CLP, such as in Lanzhou (Chen et al., 1991; Yue et al., 1992; Yue, 1995), Lantian in Xi'an (Zheng et al., 1992; Yue, 1995), Xining (Zeng et al., 1993), Beijing (Xiong et al., 2001), Baoji (Rutter et al., 1991; Yue, 1995; Yang et al., 2004), Sanmenxia (Wang et al., 2005, 2010; Zhao et al., 2006), Luochuan (Heller and Liu, 1984; Heller et al., 1987; Yue, 1995; Liu et al., 2010), Xifeng (Liu et al., 1988a; Yue, 1995), Mangshan (Zheng et al., 2007), Weinan (Pan et al., 2002). The polarity anomalies were first identified as 'Lantian normal event' (Yue, 1989; Yue et al., 1992), 'post-Jaramillo' excursions (Chen et al., 1991; Yue, 1995), or a precursor to the MB reversal (BMpc) (Zheng et al., 1992, 2007). Alternatively, Wang et al. (2005) proposed that the normal polarity zones in L9 in the Sanmenxia area were caused by remagnetization. In contrast, two normal polarity zones in L9 at the Linghui section in Baoji area (Yang et al., 2004) and at the Songjiadian section in Sanmenxia area (Wang et al., 2010) were interpreted as two excursions corresponding to Kamikatsura and Santa Rosa excursions

(Doell and Dalrymple, 1966; Maenaka, 1983), respectively. Thus, the exact details of the NRM acquisition for L9 still remain uncertain.

To resolve these ambiguities, and deepen our understanding of the paleoclimatic patterns recorded by L9, we have systematically investigated this unit at the classic Luochuan section. In previous studies, three sections (two in the Sanmenxia and one in the Baoji areas) (Wang et al., 2005, 2010; Yang et al., 2004) with available high resolution magnetostratigraphic records of L9 were all distributed in the south margin of the CLP, and located close to the Yellow River and/or the Qinling Mountain, respectively. Thus, eolian deposits would be influenced much easily by the local environment. The Luochuan section, however, is located in the Luochuan loess plateau (named 'yuan' in local) in the hinterland of the CLP, far away from high mountains and great rivers, and is most likely to faithfully preserve the paleoclimatic and paleomagnetic information.

2. Setting and sampling

The Luochuan section (35.7°N, 109.4°E) is situated in the neighborhood of Potou village, about 3 km south to the Luochuan country town. The loess-paleosol sequences (L1–L33, and S0–S32) are

~128 m thick with ~10 m of red clay underlain. In this study, we focused mainly on the unit L9 (~7.6 m thick). This unit is light yellow-gray, with sporadic small calcareous nodules. Compared to the others loess units, L9 is characterized by coarser texture and greater friability, and is marked with a relatively higher carbonate content and a relatively higher proportion of coarse silt and fine sand. There is a relatively weakly developed paleosol unit (~1.3 m thick) accompanied with moderately developed earthy carbonate in the lower part of L9. No paleosol horizons can be visually identified in the intervals of 300–750 and 880–1270 cm (in this study, the top of L8 is defined as the zero position while sampling). There is a calcareous nodule horizon (~30 cm thick) between S8 and L9.

Block samples ($5 \times 5 \times 10$ cm^3) oriented using a compass *in situ* were continuously collected. In the lab, the block samples were sawn into 2.5 cm thick slices first, and were then cut into cube specimens ($2 \times 2 \times 2$ cm^3). Two sets of oriented parallel samples were obtained (Set A and Set B, 608 specimens).

3. Experiments

3.1. Magnetomineralogical measurements

First, the low-field magnetic susceptibility (χ, mass-specific) was measured using a Bartington MS2 susceptibility meter. The anisotropy of magnetic susceptibility (AMS) was measured using a KLY-3s Kappabridge prior to thermal treatments. Anhysteretic remanent magnetization (ARM) was imparted using an alternating field (AF) with a peak of 100 mT superimposed on a 0.05 mT direct current biased field using a Model615 anhysteretic remanent magnetizer. The ARM is expressed in terms of the ARM susceptibility (χ_{ARM} = ARM/DC field). Isothermal remanent magnetization (IRM) was acquired in a DC field using a 2G660 pulse magnetizer with 2.7 T (defined as saturation IRM, SIRM) and 100, 300 mT back fields (IRM$_{-0.1 \text{ T}}$ and IRM$_{-0.3 \text{ T}}$, respectively). The S-ratio (defined as $-$IRM$_{-0.3 \text{ T}}$/SIRM) and the hard IRM (HIRM, defined as $0.5 \times$ (SIRM + IRM$_{-0.3 \text{ T}}$)) were calculated to quantify the relative and absolute concentrations of antiferromagnetic minerals (e.g., hematite and goethite). The L-ratio (defined as HIRM/ ($0.5 \times$ (SIRM + IRM$_{-0.1 \text{ T}}$))) was used to further evaluate the interpretation of S-ratio and HIRM (Liu et al., 2007). The SIRM was subsequently AF demagnetized to peak fields of 30, 60, 100 mT, respectively. Accordingly, the residual magnetization refers to SIRM$_{30}$, SIRM$_{60}$, and SIRM$_{100}$, respectively. SIRM$_{100}$/SIRM was calculated to observe the relative content of hematite in bulk samples (Deng et al., 2006). All remanences were measured using a 2G Enterprises Model 760 cryogenic magnetometer installed in a magnetically shielded room (residual fields <300 nT).

Six representative samples corresponding to the peaks and troughs of the grain size curves at 247.5, 387.5, 512.5, 665, 825, and 1035 cm were selected for further rock magnetism measurements. Temperature-dependent susceptibility (χ–T) curves were measured using a KLY-3s Kappabridge equipped with a CS-3 high-temperature furnace going from room temperature up to 700 °C in an argon atmosphere (the flow rate is about 100 ml per minute). Hysteresis parameters, including the saturation magnetization (M_s), saturation remanence (M_{rs}), coercivity (B_c), coercivity of remanence (B_{cr}), IRM acquisition curves (with a maximum field of 2 T) were measured with a Princeton Measurements vibrating sample magnetometer (VSM3900).

3.2. Paleomagnetic measurements

Progressive thermal demagnetization of NRM was carried out on the Set A samples (314 specimens) from room temperature up to 680 °C to determine the characteristic remanent magnetization (ChRM) using a Magnetic Measurements Thermal Demagnetizer (MMTD80) with a residual field of <10 nT. The Set B samples (302 specimens) were stepwise AF demagnetized to a peak field of 100 mT.

To monitor the characteristics of hematite as a possible ChRM carrier, combined demagnetization methods were performed on pivot samples. After AF demagnetization, about 80 samples were additionally thermal demagnetized from 600 to 680 °C.

3.3. Low-temperature demagnetization of the NRM and ChRM

To determine the exact carriers of the NRM and ChRM, low-temperature demagnetization (LTD) of these two remanences were performed on a Quantum Designs single axis superconducting quantum interference device (SQUID) Magnetic Properties Measurement System (MPMS). Two representative samples at 387.5 and 825 cm were selected. Remanences directions of the NRM and the ChRM were first determined with oriented cubic specimens after progressive thermal demagnetization. Then, small cylindrical samples (~0.5 cm in diameter and ~1.5 cm in length) were cut from the sister cubic samples without thermal treatment along the directions of NRM and ChRM, respectively. Two sub-samples were obtained for each sample: one for the NRM-LTD, the other for the ChRM-LTD which was first thermal demagnetized at 300 °C (held 40 min) using the MMTD80 before LTD. Prior to LTD measurements, the ambient field in the measurement chamber of the MPMS was adjusted to <±0.5 μT. Then samples were cycled in a zero field from room temperature to 50 K with temperature steps of 5 K between 50–90 K and 130–300 K, and of 2 K between 90 and 130 K. Finally, two sub-samples for NRM-LTD were given a LT-SIRM, in which an IRM acquired in a 2.5 T field at 10 K after a zero field cooling from 300 K. The LT-SIRM demagnetization was measured during warming from 10 to 300 K. The measured remanent magnetizations of samples were much higher than the background caused by the empty plastic straw holders. Therefore, the effect of the background could be neglected and the measured LTD curves could reflect the behaviors of the remanence carriers.

3.4. Non-magnetic measurements

The particle size of 381 bulk samples was measured with a SALD-3001 laser diffraction particle analyzer. Ultrasonic pretreatment with the addition of 20% (NaPO$_3$)$_6$ solution was used to disaggregate the samples before measurement. Replicate analysis showed a precision of <5% for this procedure. Magnetic extracts were taken from the parallel samples at 387.5, 665, 825, and 1035 cm in order to investigate the morphology and source of magnetic particles of L9, using a model LEO1450VP scanning electron microscope (SEM). The sample was diluted in water followed with sufficiently disaggregation with ultrasonic treatment. Then, the magnetic extract was manually performed using a high-gradient magnet.

4. Results

4.1. Magnetic susceptibility and particle size

Consistent with previous studies, the χ values show prominent peaks for the two well developed paleosol horizons, S8 and S9, with an average of 113.2×10^{-8} m^3/kg and 102.5×10^{-8} m^3/kg, respectively (Fig. 2b). In contrast, the χ curve for L9 is relatively smooth with an average of 31.4×10^{-8} m^3/kg. The weakly developed paleosol horizon in the 755–880 cm interval corresponds to a moderate χ peak, with an average of 50.9×10^{-8} m^3/kg which is larger than the χ average of L9, but is only about half of that

for S8 or S9. The χ average of L8 (47.9×10^{-8} m^3/kg) is also higher than that of L9.

Coarse lithogenic magnetic minerals may be controlled by the extent of source areas and/or wind system, and local source materials have also been documented to influence the magnetic susceptibility (Sun and Liu, 2000a). However, the latter mechanism will not dominate the susceptibility in the Luochuan area, which is situated far from the source areas, such as the Gobi and desert regions in inland Asia (Sun and Liu, 2000a; Sun and Huang, 2006). Therefore, the susceptibility in Luochuan is relatively sensitive to pedogenesis, but not to source changes, and can be defined as a proxy of the strength of east-Asian summer monsoon (An et al., 1991; Sun and Huang, 2006).

Four sediment fractions, <2, 2–20, >20 μm, and median grain size (Md) are shown in Fig. 2c–f. The former two fractions have similar pattern with higher percentages for S8 and S9 (Fig. 2c and d), which is consistent with susceptibility changes. The Md and >20 μm fraction have an opposite pattern (Fig. 2e and f). The fine silt fraction (2–20 μm) accounts to 33–51% for S8 and 38–51% for S9, and only 23–45% for L9. The >20 μm fraction accounts to 26–50% for S8 and 27–44% for S9, but a higher percentage for L9 (35–66%). The Md of S8 ranges from 8 to 20 μm, with an average of 11 μm and 9–12 μm for S9 with an average of 11 μm. The L9 has a wider Md range (10–31 μm) with an average of 17.6 μm. The L9 particle size curves show more fluctuations than susceptibility, such as the peaks (or troughs) in the intervals of 470–600 and 755–880 cm (Fig. 2b–d). The latter interval corresponds to the weak soil horizon, but there is no visible evidence for the presence

of a soil horizon in the 470–600 cm interval. Therefore, the Md curve is more sensitive to paleoclimatic changes in this region than susceptibility.

Particles in the size range of 2–20 μm are always long-range transported dust, mainly derived from remote dust source regions by long-term suspension (Sun and Liu, 2000b). The >20 μm fraction can only be transported by short-term suspension and saltation for short distances, on the order of 30 to hundreds of kilometers (Tsoar and Pye, 1987; Sun and Liu, 2000b; Sun and Huang, 2006). Therefore, the troughs of Md and >20 μm fraction, or the peaks of 2–20 μm indicate the periods of decreased winter monsoon wind energy (Liu and Ding, 1998; Sun and Liu, 2000b; Ding et al., 2002; Sun and Huang, 2006), such as the intervals of 470–600 and 755–880 cm, although the clay fraction of <2 μm is mainly generated during pedogenic process (Liu, 1985; Hao et al., 2008), such as for S8, S9, and the interval of 755–880 cm. Due to the absence of pedological evidences, the peak of the <2 μm fraction in the 470–600 cm interval is mainly attributed to the source origin. The clay fraction may be transported by adhering to the surface of silt grains, or as silt-sized aggregates from source regions, which also reflects a decreased winter monsoon (Liu, 1985; Derbyshire et al., 1995).

4.2. Magnetic mineralogy

The χ–T curves for samples at 387.5, 512.5, 665, and 1035 cm exhibit a major decrease at about 585 °C, which indicates the presence of magnetite (Fig. 3a). The slight increases up to 250 °C have
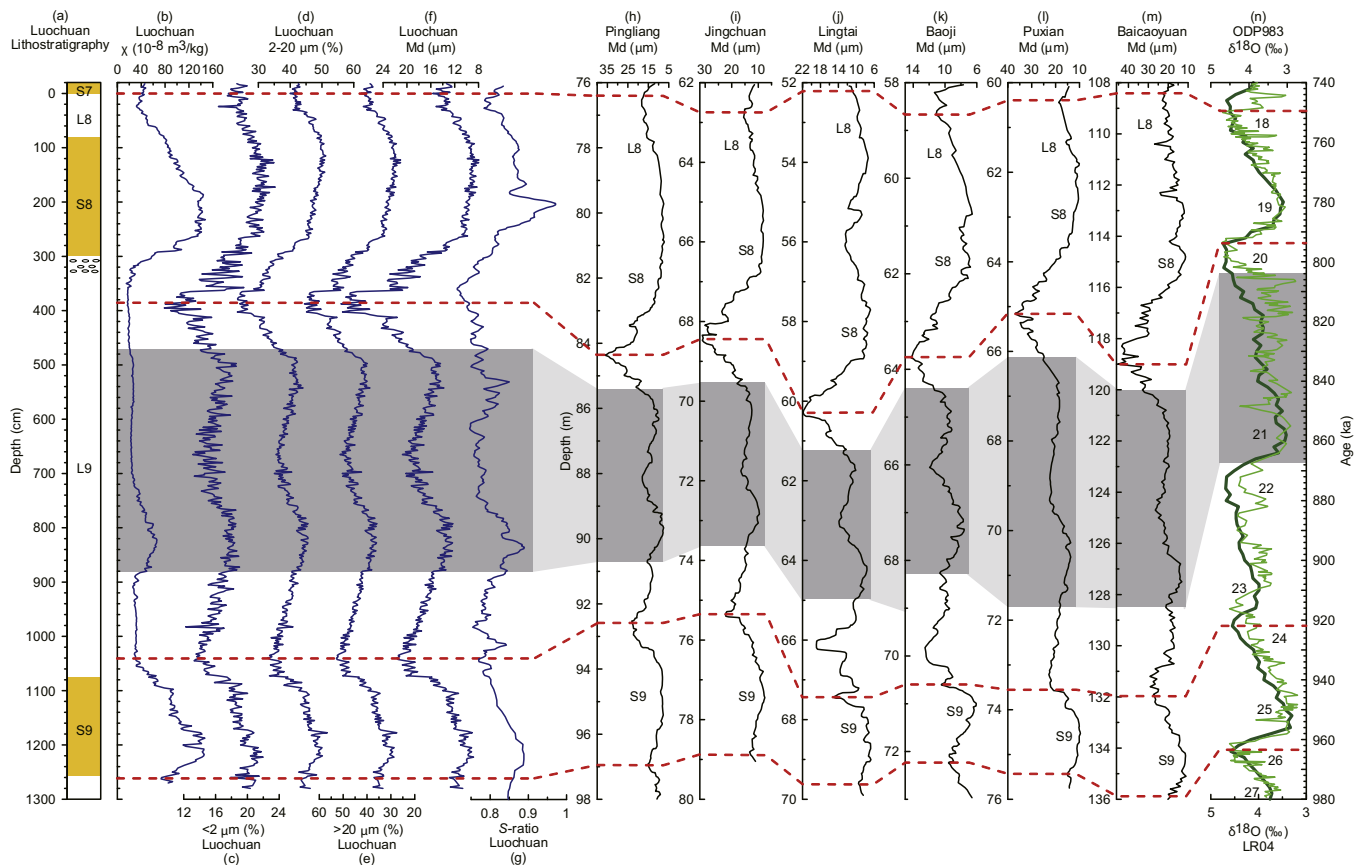

Fig. 2. Pedostratigraphy and climatostratigraphy from L8 to S9 at Luochuan section, and correlation with records in other loess sections and marine oxygen isotope. (a) Lithostratigraphy, ellipses represent a calcareous nodule horizon; (b) mass-specific low-field magnetic susceptibility (χ); (c–f) components of bulk grain size; (g) S-ratio; (h–m) Md for Pingliang, Jingchuan, Lingtai, Baoji, Puxian, and Baicaoyuan sections. Data for the former five sections are from Ding et al. (2002); (n) δ^{18}O data are from ODP983 (Channell and Kleiven, 2000) and LR04 (thicker line) (Lisiecki and Raymo, 2005). The numbers are the marine oxygen isotope stages. Dashed lines represent climatic control points. A climatic optimum is shaded.
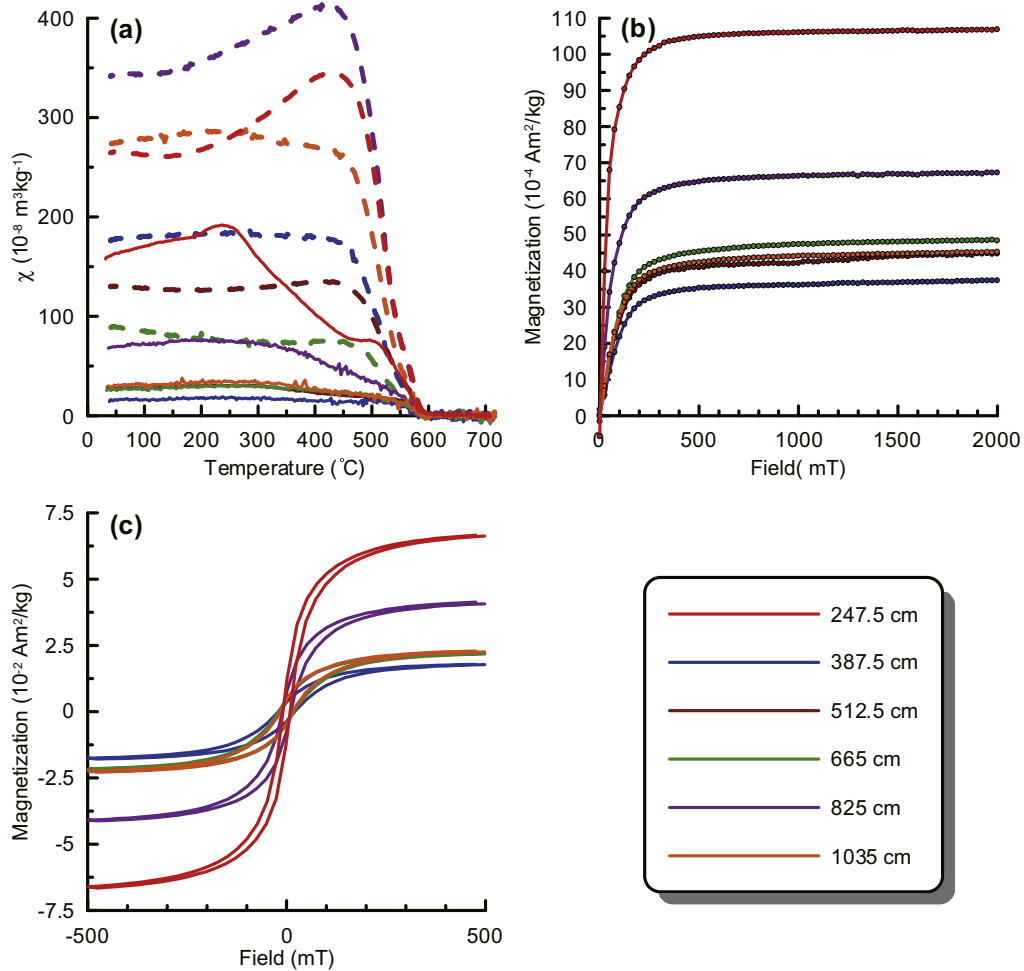
Fig. 3. Rock magnetism results for the six selected samples. (a) Temperature-dependent susceptibility curves. Solid (dashed) lines represent heating (cooling) processes; (b) isothermal remanent magnetization (IRM) acquisition curves; (c) hysteresis loops.

been generally attributed to the gradual unblocking of fine ferromagnetic particles (near the superparamagnetic/single domain boundary) (Liu et al., 2005b; Deng, 2008). The steady decreases after 300 °C is generally interpreted as the conversion of metastable maghemite to weakly magnetic hematite (Deng et al., 2000, 2004, 2005, 2006; Deng, 2008; Liu et al., 2005b; Jin and Liu, 2010). This behavior is more evident for samples from S8 than from L9, indicating increased maghemite production due to enhanced pedogenesis (Deng et al., 2000). The heating curve for the sample at 825 cm from the weak soil horizon displays intermediate magnetic behaviors relative to the sample at 247.5 cm from S8 and samples from L9. Another notable characteristic of the χ–T curves is that they are irreversible below about 600 °C during cooling. The χ after cooling is always several times higher than the initial values before heating, which is generally attributed to the neoformation of magnetite grains from iron-containing silicates/clays, or due to the formation of magnetite by reduction as a result of the burning of organic matter (Hunt et al., 1995; Deng et al., 2000, 2004, 2005, 2006, 2008; Liu et al., 2005b).

The IRM acquisition curves have similar shapes for all samples (Fig. 3b). IRM climbs rapidly below 200 mT and reaches approximate saturation at about 300 mT. This behavior reveals the existence of soft magnetic minerals, such as magnetite and/or maghemite. For loess samples, the IRM curves show slight increases from 300 mT up to 2 T, indicating the presence of hard magnetic components, such as hematite and/or goethite. SIRM is enhanced with the development of pedogenesis.

After subtracting the distinct paramagnetic contribution in high field, all the hysteresis loops are closed by about 300 mT (Fig. 3c), further displaying behaviors of soft magnetic components, consistent with the IRM results. A weakly wasp-waisted shape indicates a mixture of magnetic minerals with low and high coercivities. The M_s shows an increased pattern depending on the enhanced pedogenesis, contrary to the changes of B_c and B_{cr}.

Environmental magnetism parameters for samples in the 290–1110 cm interval are shown in Fig. 4. The average S-ratio for L9 is 0.8, which indicates that the dominant magnetic carrier is magnetite (Fig. 4h). Almost all the parameters have distinct troughs or peaks for the interval of 755–880 cm, which corresponds to the weak soil horizon. In the 470–600 cm interval, the magnetic enhancement is evidenced by χ, χ_{ARM}, and SIRM curves (Fig. 4a–c), and more by M_s and S-ratio curves (Fig. 4d and h), indicating an increased magnetite concentration relative to the intervals of 350–470, 600–750 and 880–1050 cm. The L-ratio is almost constant for L9 (Fig. 4j). Therefore, the HIRM could be recognized as the 'absolute' concentration of hematite (Liu et al., 2007) (Fig. 4i), which varies in phase with magnetite content (Fig. 4k and l) as well as coercivity changes (Fig. 4n and o) and the relative content of hematite (Fig. 4m). Owing to a weak pedogenesis effect during the deposition of L9 which makes against the new pedogenic formation of hematite, the hematite particles were mainly derived from source areas. Therefore, the lower concentration of hematite in the 470–600 and 755–880 cm intervals (Fig. 4i and m) strongly indicates a decrease in the strength of the
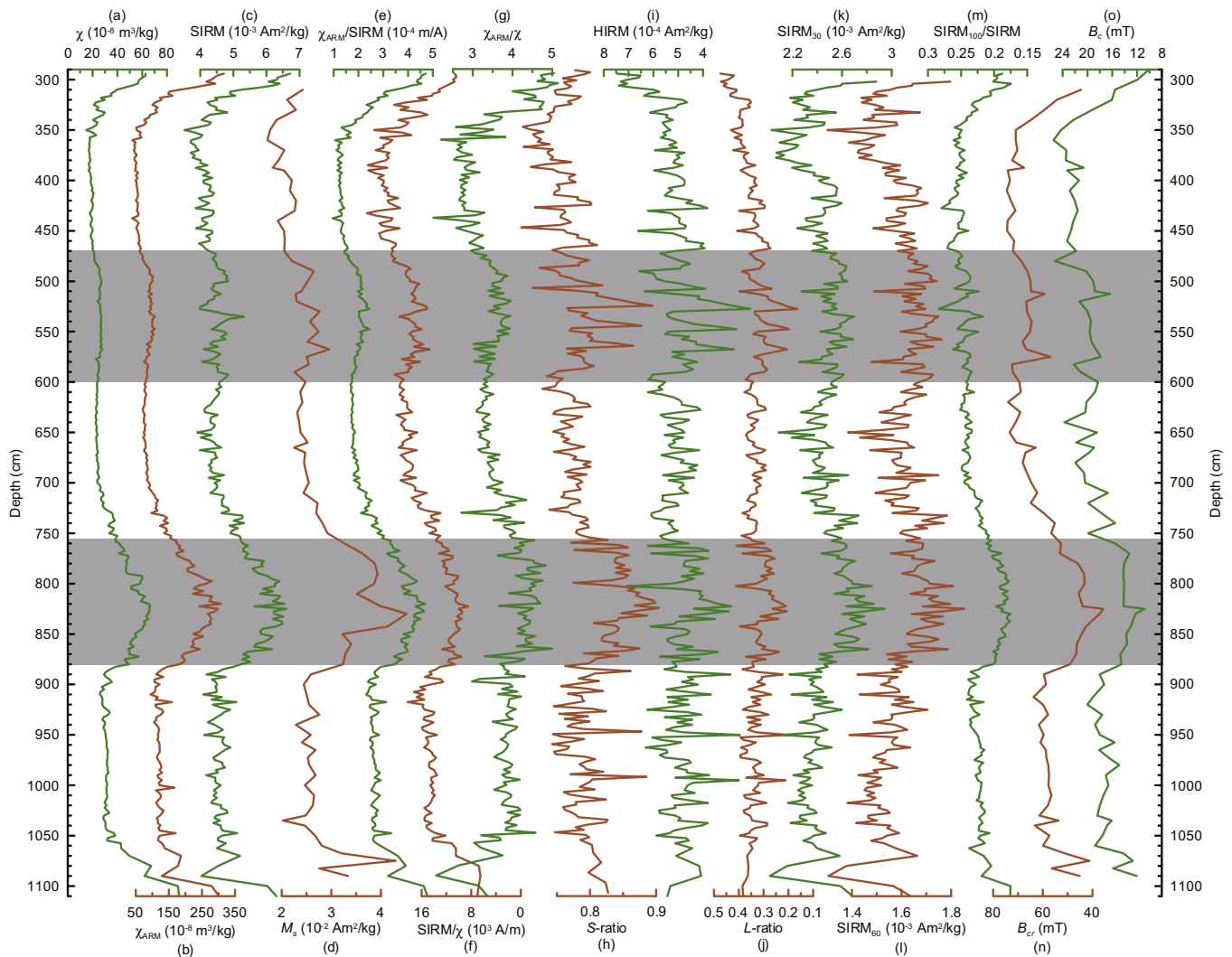
Fig. 4. Magnetic mineralogical parameters. The gray shading represents periods of decreased east-Asian winter monsoon strength.

winter monsoon, which is consistent with results of bulk grain size.

4.3. Magnetic grain size

Ratios of χ_{ARM}/SIRM, SIRM/χ, and χ_{ARM}/χ can be used as grain size indicators for magnetite (Evans and Heller, 2003) and were widely employed in loess studies (Bloemendal and Liu, 2005; Deng et al., 2005, 2008; Wang et al., 2005). These three ratios display similar pattern (Fig. 4e–g). Higher values of χ_{ARM}/SIRM and χ_{ARM}/χ and lower values of SIRM/χ in the 470–600 and 755–880 cm intervals are indicative of finer magnetic grain size compared with intervals of 350–470, 600–750 and 880–1050 cm. The decreased magnetic grain size in the 470–600 cm interval is also attributed to the decreased winter monsoon strength. However, the finer magnetic components in the 755–880 cm interval may be a combination of enhanced pedogenesis and decreased winter monsoon.

The results of SEM of the four studied samples indicate that the magnetic grains of the four samples have fractured edges and corners, and are poorly sorted (Fig. 5). The magnetic grain size ranges from a few microns to 42 μm for the sample at 387.5 cm (corresponding to the maximum of the Md curve) with an average of 20.2 μm (Fig. 5a), and ranges from 1 to 20.5 μm for the sample at 825 cm (corresponding to the minimum of the Md curve) with

an average of 12 μm (Fig. 5c). The average size for samples at 665 and 1035 cm are 14.7 and 19.6 μm, respectively (Fig. 5b and d). The large size and generally irregular shapes of the extracts suggest that they are of aeolian origin. According to the calculation of Tsoar and Pye (1987), dust particles of <20 μm can be transported in long-term suspension over a greater height range and may be widely dispersed, but the >20 μm particles can only be transported to a shorter distance (∼30 to hundreds of kilometers). Therefore, the coarse magnetic particles of L9 were mainly transported from a proximal source area. The changes of magnetic grain size are in phase with bulk grain size depending on pedostratigraphy. Therefore, the Md may be considered to an approximation, as a grain size proxy of detrital magnetic particles in this study.

4.4. LTD of the NRM and ChRM

The LT-SIRM, LTD-NRM, and LTD-ChRM curves for the two representative samples are shown in Fig. 6. Both the samples display distinct Verwey transitions (T_v, 110–120 K) in LT-SIRM curves which is indicative of coarse-grained magnetic particles (e.g., MD and/or large PSD) (Dunlop and Özdemir, 1997) (Fig. 6a and b). Based on the first derivatives of the LT-SIRM curves, this behavior is more evident for the sample at 387.5 cm than that at 825 cm, which indicates coarser magnetic grain size.
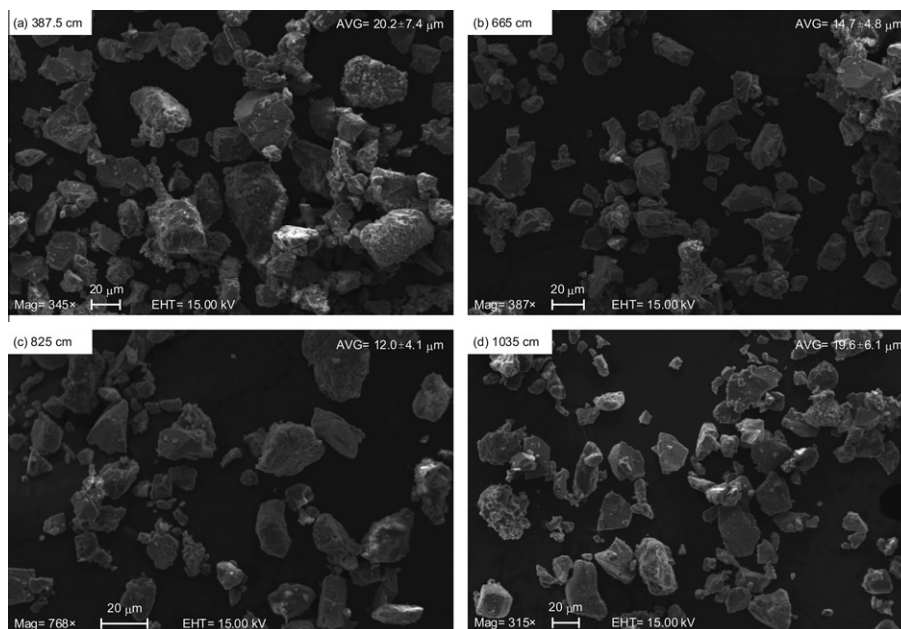
Fig. 5. Morphology of extracted magnetic particles for the four selected samples at 387.5, 665, 825, and 1035 cm, observed using a scanning electron microscope.

For the sub-samples at 387.5 cm, the NRM intensity increases steadily from room temperature to about 140 K during cooling, then the NRM intensity decreases sharply from 140 to 120 K (Fig. 6c). On cooling through T_v, the intensity increases again. On the warming curve, the intensity is reversible up to 130 K, then deviates from the cooling curve and reaches a peak at 140 K. It decreases between 140 and 240 K, and keeps almost constant till to 300 K. The LTD-ChRM curves are similar to the LTD-NRM curves. The ChRM intensity gradually increases up to 130 K, and then decreases (Fig. 6e). On the warming curve, the intensity is reversible below 120 K, and then deviates from the cooling curve. It decreases from 120 to 210 K and remains approximately constant between 210 and 300 K.

For the sample at 825 cm, the LT behavior differs significantly from that of the sample at 387.5 cm. The NRM intensity approximately increases from 300 to 50 K during cooling curve with a slightly identified concavity between 135 and 120 K (Fig. 6d). The warming curve departs from the cooling curve after about 130 K and steadily decreases till to 300 K. The ChRM intensity increases gradually to 130 K from room temperature and sharply increases between 135 and 115 K (Fig. 6f). It is reversible before 140 K.

4.5. Paleomagnetic results

Principal component analysis, calculated by a least-squares fitting technique (Kirschvink, 1980) was carried out on the demagnetization data using the PaleoMag software (version 3.1d40) developed by Craig H. Jones and Joya Tetreault. Orthogonal projections of representative samples are shown in Fig. 7, with samples recording both normal (Fig. 7a–d, g and k) and reverse (Fig. 7e and f) polarity, respectively. Two components in demagnetization curves can be identified for reverse samples (e.g., Fig. 7e and f). The low-temperature component of the NRM is eliminated by demagnetization to 300 °C, with a mean direction (after Fisher statistics, 1953) of Declination = 351°, Inclination = 55.9° (α_{95} = 0.9, n = 296), closed to the present-day geomagnetic field (Dec = 356.6°, Inc = 53.8°) and to the present geocentric axial dipole field (Inc = 55.2°) in the sampled site. The consistency between the low-temperature component, and the present field strongly indicates viscous remanent magnetization (VRM) origin

(e.g., Pan et al., 2001; Wang et al., 2005). A single magnetic component, parallel to the present geomagnetic field, is present in samples with normal polarity (e.g., Fig. 7a–d, g and k). No stable magnetic components are present at temperatures >585 °C, which indicates that hematite does not contribute to the ChRM (e.g., Fig. 7j and k). Many samples that record a reverse polarity, as resolved by thermal demagnetization, cannot be adequately AF demagnetized, such as samples from 825 cm (Fig. 7e and h) and 895 cm (Fig. 7f and i). This behavior indicates that the VRM components of these samples may be carried not only by ferromagnetic minerals but also by high-coercivity ones (Heller et al., 1987). In addition, this behavior may be attributed to low-temperature oxidation of detrital magnetite particles which can significantly increase the coercivity of coarse-grained partially oxidized magnetite particles due to the stresses created by the mismatching of the unit cell between the maghemite rim and the magnetite core (vanVelzen and Dekkers, 1999; Liu et al., 2002, 2003a, 2004a, 2004b, 2005a).

Finally, the ChRM were determined by at least four continuous demagnetization steps always between 300 and 550 °C with a maximum angular deviation <15°. Combining rock magnetism and SEM results, we can conclude that the ChRM is dominantly carried by coarse-grained (large PSD and/or MD) partially oxidized magnetite particles.

Five magnetic abnormal zones are observed in L9. Thereinto, anomalies 1, 3, and 5 are normal polarity zones, and 2, 4 display magnetically chaotic behaviors (Fig. 8b and d–f). NRM300 (NRM after 300 °C thermal demagnetization) divided by SIRM was normalized to evaluate the potential remanences (Fig. 8g and h).

4.6. AMS results

The AMS results, especially the inclination of the maximum-susceptibility axis (K_{max}-Inc) and minimum-susceptibility axis (K_{min}-Inc), have been widely used in loess studies to detect possible disturbance of the original sediment fabric and to test the reliability of NRM recording (Liu et al., 1988b, 2005a; Zhu et al., 1994a, 1999, 2004; Guo et al., 2001, 2002a; Wang et al., 2005, 2010; Yang et al., 2007, 2010). The K_{max}-Inc, K_{min}-Inc, degree of AMS (P) and AMS ellipsoid shape (T) are shown in Fig. 9. Two sets of parallel
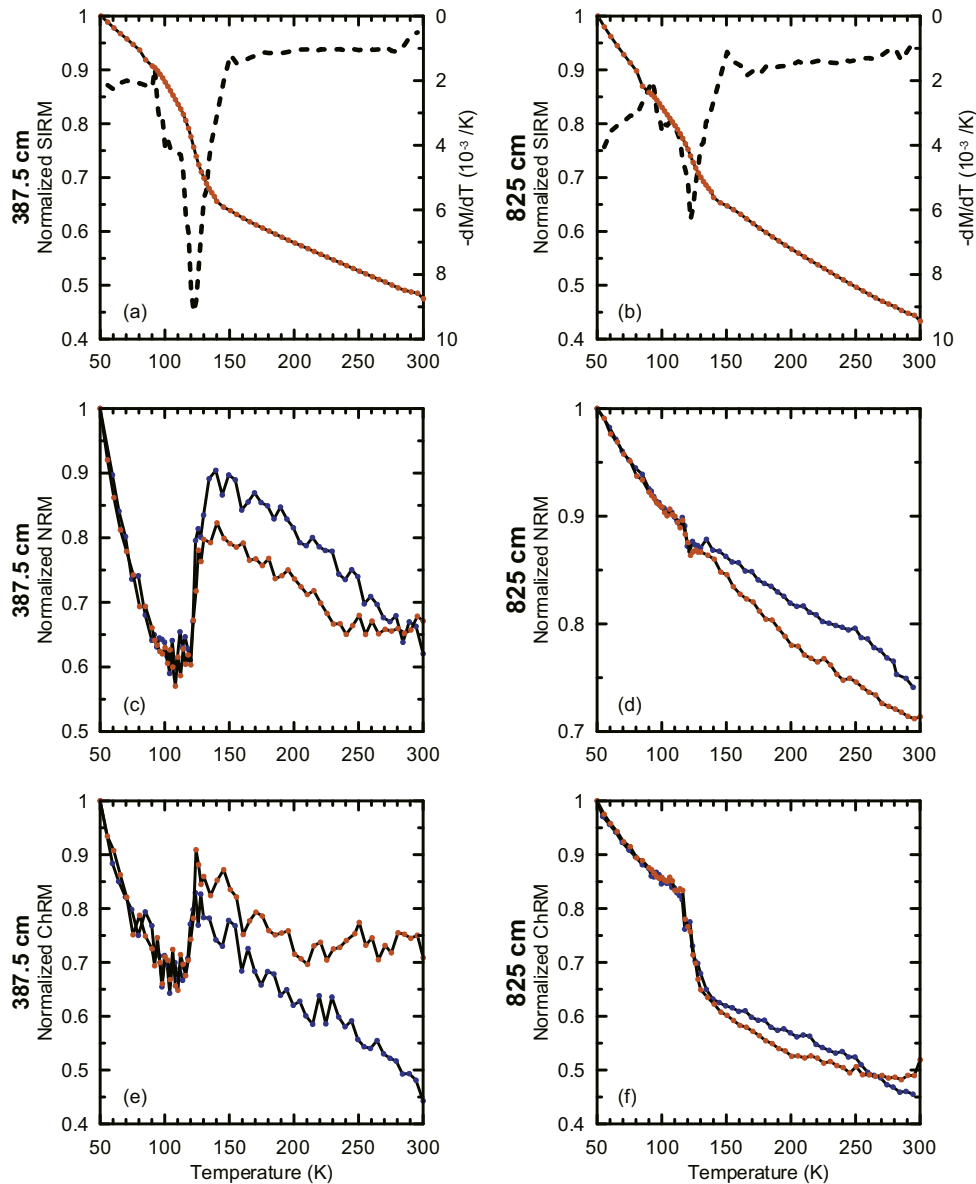
Fig. 6. Low-temperature (LT) magnetic characteristics for samples at 387.5 and 825 cm. (a) LT-SIRM. Dashed lines are the first derivatives of LT-SIRM curves; (b) LT demagnetization (LTD) of the natural remanent magnetization (NRM); (c) LTD of the characteristic remanent magnetization (ChRM). Blue (orange) lines indicate cooling (heating) courses. (For interpretation of the references to color in this figure legend, the reader is referred to the web version of this article.)

samples have consistent AMS features. The average of foliation and lineation are 1.01 and 1.001, respectively, for both subsets of samples, which indicates that the susceptibility ellipsoid is oblate shaped, associated with $T < 1$ (Fig. 9c and g). With exception of the top 45 cm, K_{max}-Inc is less than 15° (97% <10°, 81% <5°), approximately parallel to the horizontal plane (Figs. 9a and e, and 10). K_{min}-Inc is larger than 70° (94% >80°), approximately perpendicular to the horizontal plane (Figs. 9b and f, and 10).

These data indicate a primary sediment fabric without evident disturbance after dust deposition. P (<1.02) is obviously less than 1.032, which has been suggested as the critical value between redeposited loess and original loess by Liu et al. (1988b), further indicating an original fabric. However, a special AMS zone has been identified in the 330–375 cm interval which is indicative of larger K_{max}-Inc and shallower K_{min}-Inc. This distorted fabric may be caused by sediment disturbance, such as the rotation of the magnetite particles forced by rainfall infiltration during S8 period.

5. Discussion

5.1. Construction of a new age model for L9

To determine the exact mechanism that records polarity anomalies in L9, an accurate age model is essential. Although large scale lock-in depth for NRM in Chinese loess (~2–3 m) has been suggested for resolving the discrepancy of the polarity boundaries recorded in loess and marine sediments (Zhou and Shackleton, 1999; Heslop et al., 2000; Spassov et al., 2003), more pieces of evidence support a small NRM lock-in depth in Chinese loess (Zhu et al., 1994a, 1998, 2006; Pan et al., 2002; Wang et al., 2006; Yang et al., 2008, 2010; Jin and Liu, 2010). Sedimentological redeposition experiments suggested that the capability of the deposited loess dust to acquire a post-detrital remanent magnetization (pDRM) is enhanced with water content in sediments (Zhao and Roberts, 2010). Magnetic particles as ChRM carriers in the deposited dusts
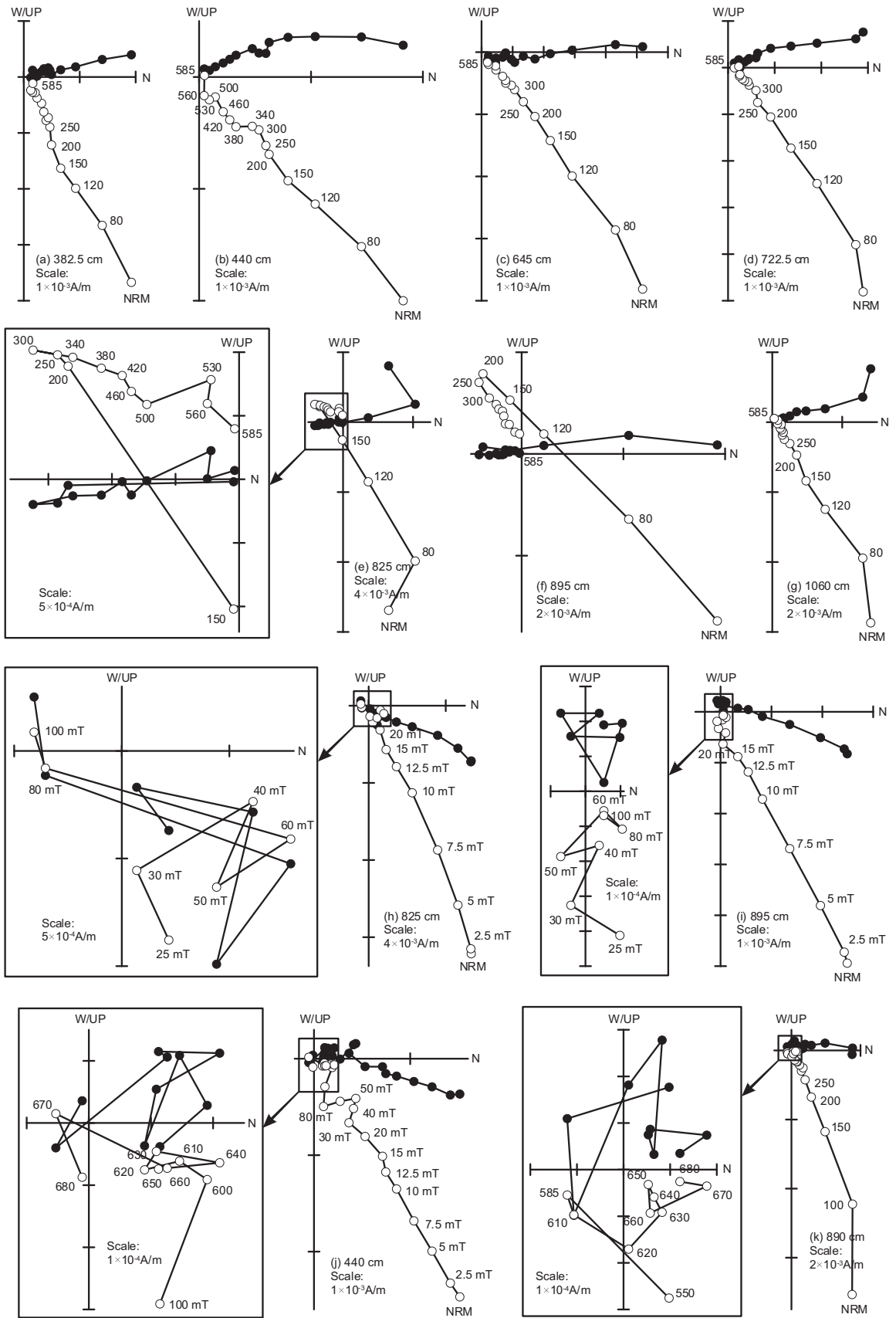
Fig. 7. Orthogonal projections of progressive thermal and alternating field demagnetization of the NRM for representative samples. Shaded and open circles represent projections onto the horizontal and vertical plane, respectively. Demagnetization temperature is given in degrees Celsius.
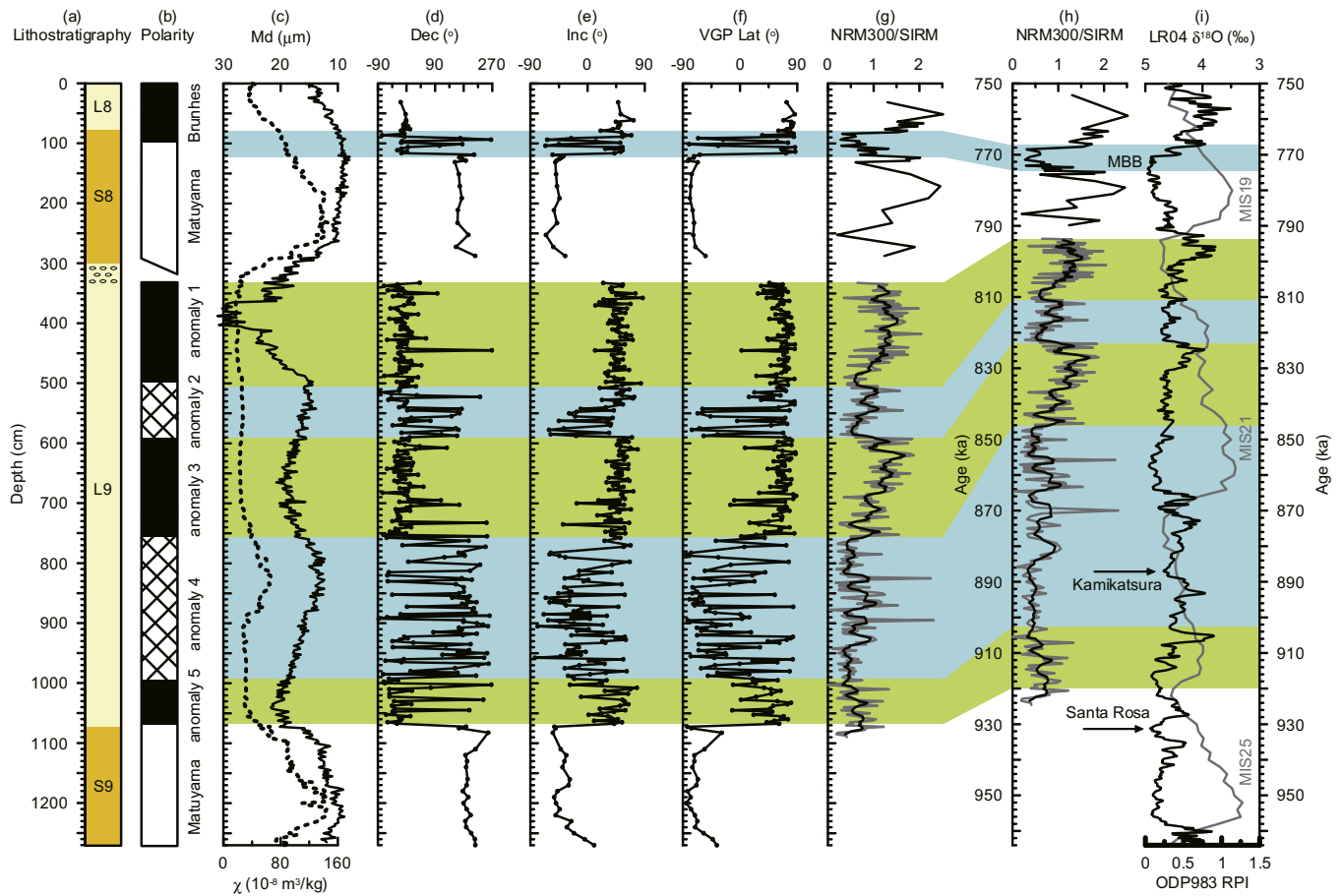
Fig. 8. (a) Pedostratigraphy; (b) magnetic polarity; (c) low-field susceptibility (dashed line) and Md curve (solid line); (d) declination (Dec) of the ChRM; (e) inclination (Inc) of the ChRM; (f) virtual geomagnetic pole latitude (VGP Lat); (g) NRM after 300 °C thermal demagnetization normalized by SIRM (NRM300/SIRM); (h) time-dependent NRM300/SIRM. The dark line is a 5 points running average; (i) relative paleointensity (RPI) data are from ODP983 (dark line; Channell and Kleiven, 2000) and $\delta^{18}O$ from LR04 (gray line; Lisiecki and Raymo, 2005).

can be fixed permanently along the ambient field after the initial wetting (Wang and Løvlie, 2010). The moisture of the sedimentary environment associated with rainfall in the CLP determined a shallow lock-in model in Chinese loess, which is also represented by the short-period paleomagnetic events recorded in loess, such as excursions (e.g., Zhu et al., 1994b, 1999, 2006, 2007; Zheng et al., 1995; Fang et al., 1997; Pan et al., 2002; Yang et al., 2007). Thus the downward displacements of the polarity boundaries in loess may be limited to only several centimeters due to high sediment rates and shallow NRM lock-in depth (Liu et al., 2008), associated with a limited surface mixing layer (~5 cm) (Sun et al., 2010b). Therefore, these polarity boundaries could be considered as accurate age controls and can be faithfully correlated with those in marine sediments.

The most recent magnetostratigraphic results of Liu et al. (2010), with a sampling resolution about 10 cm, revealed that the transitional zone between the Matuyama and the upper boundary of Jaramillo was about 40 cm thick, with a midpoint located in the paleosol unit S10 (Fig. 11a). This is consistent with results of Heller and Liu (1984), Kukla and An (1989), Zheng et al. (1992), Guo et al. (2002a), Pan et al. (2002), Wang et al. (2005), and Wang et al. (2010). In marine sediments, the upper boundary of Jaramillo is located in MIS 27 (Ruddiman et al., 1989; Shackleton et al., 1990; Channell and Kleiven, 2000; Channell et al., 2002; Channell and Raymo, 2003) (Fig. 11c). Therefore, S10 can be confidently correlated to MIS 27. Then, the overlying units L10 and S9 can be correlated to MIS 26 and MIS 25, respectively, consistent

with results of Wang et al. (2006). Because the paleosol unit S8 is tied to MIS 19 (Wang et al., 2006; Liu et al., 2008; Jin and Liu, 2010), the whole L9 should cover MIS 20–24 (Fig. 11).

In the Luochuan region, a weak soil horizon (755–880 cm) can be easily identified in the field outcrop. This horizon indicates decreased winter monsoon strength and enhanced summer monsoon (Fig. 2b–g). Meanwhile, another interval (470–600 cm) also corresponding to a period of decreased winter monsoon was identified on the basis of climatological proxies (Figs. 2 and 3). These two major troughs in the Md curves of L9 can be widely identified across the CLP (Fig. 2h–m). An additional Md trough can also be identified in the intervals of ~68.2–69.2 m at Baoji section and ~91–92 m at Pingliang section (Fig. 11b), as well as at ~65.5 m at Lingtai section (Fig. 2j) and 131 m at Baicaoyuan section (Fig. 2m). This trough indicates a relatively moderate environment although weaker in magnitude than the trough in the intervals of ~1–5 m upon in different areas. This inconsistency between sections may be attributed to sedimentary discontinuity in the Luochuan region (e.g., Ding et al., 2002; Zhu et al., 2007; Deng, 2008) and/or the influences of local environment during dust deposition in different areas of the CLP, especially local paleoprecipitation, which has an effect on pedogenesis in some extent (Maher and Thompson, 1995; Hao and Guo, 2005; Liu et al., 2005a). Nevertheless, on the basis of the overall Md pattern over a wide area of the CLP, three Md troughs are recorded in L9. The upper two and the lower Md troughs can be correlated to MIS 21 and 23, respectively. Such a correlation is consistent with the paleoclimate pattern. Among
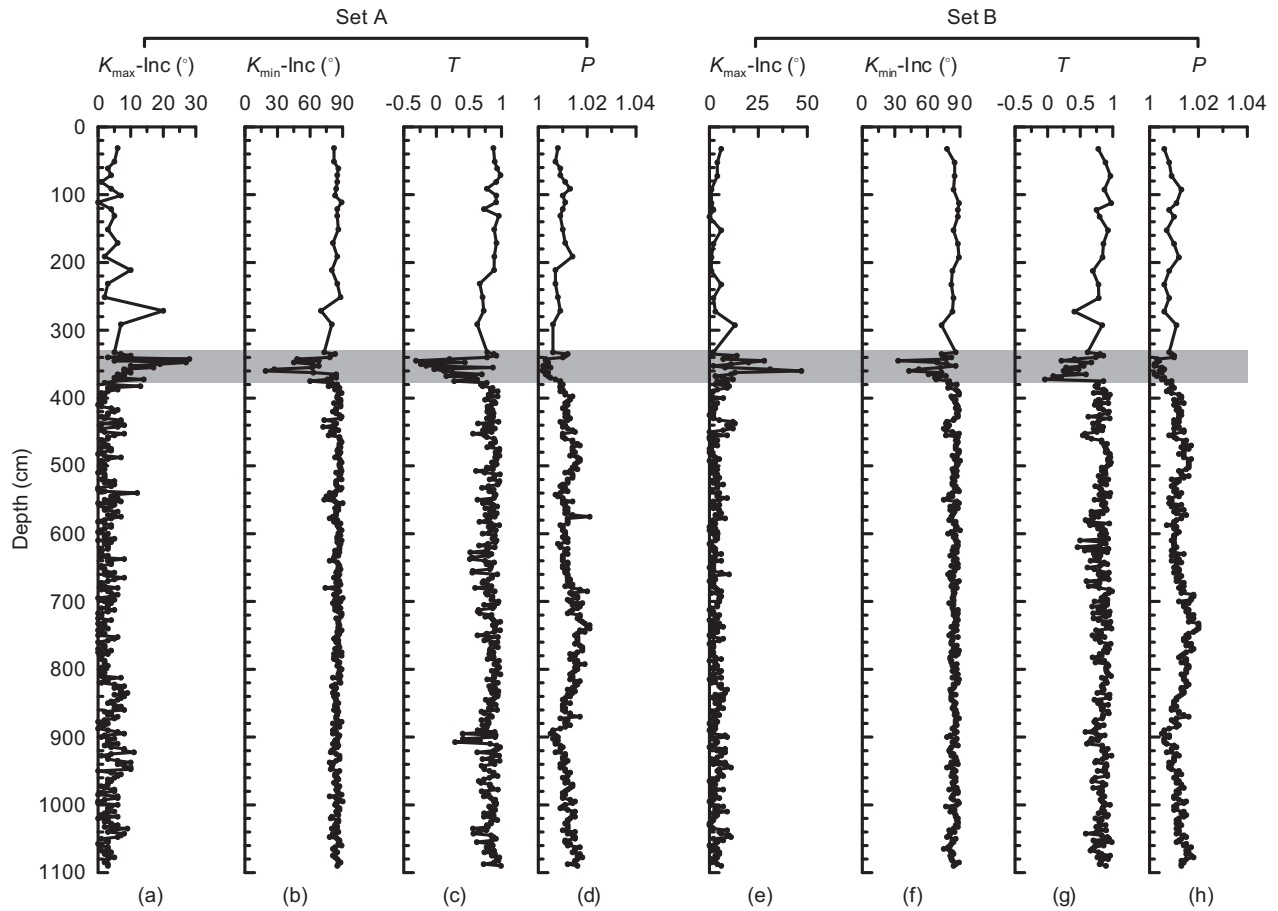
Fig. 9. The anisotropy of magnetic susceptibility (AMS) for the two sets of parallel oriented cubic samples. (a and e) inclination of maximum-susceptibility axis (K_{max}-Inc); (b and f) inclination of minimum-susceptibility axis (K_{min}-Inc); (c and g) AMS ellipsoid shape (T); (d and h) degree of AMS (P). An AMS chaotic zone is shaded.
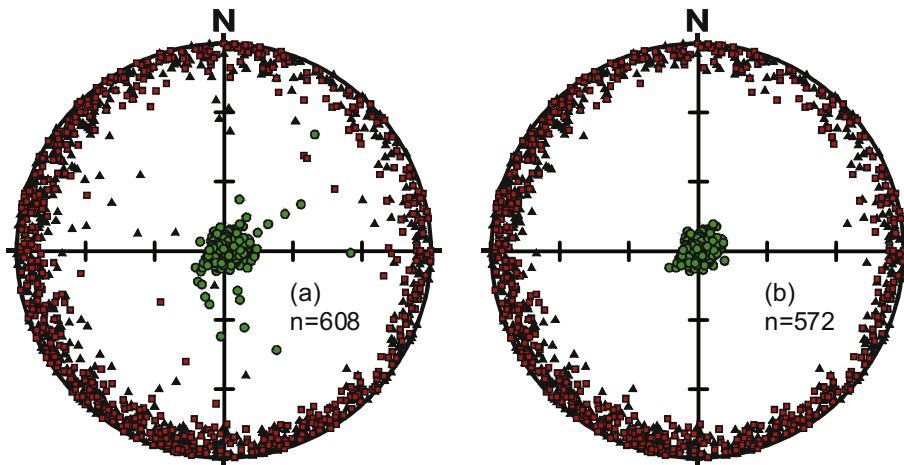

Fig. 10. AMS principal directions in an equal-area stereographic projection. Squares, triangles, and circles represent maximum, intermediate, and minimum-susceptibility axis, respectively. (a) all samples. (b) Samples in the top 45 cm of L9 are excluded.

MIS 21 and 23, the older part of MIS 21 corresponds to the warmest period, and thus it is most reasonable to tie the weak soil unit in L9 to such a warm period.

On the basis of the tie points from both the geomagnetic reversal boundaries and paleoclimatic boundaries (Figs. 2 and 11), an age model for the units S8 and L9 is constructed through linear interpolation and shown in Fig. 8h. Based on

the new age model, the three short paleomagnetic normal chrons within L9 (anomalies 1, 3 and 5) do not correspond to the paleomagnetic excursions recorded in the marine sediments (e.g., Kamikatsura and Santa Rosa excursions; Doell and Dalrymple, 1966; Maenaka, 1983). Our results therefore support that these polarity anomalies are caused by the remagnetization of NRM.
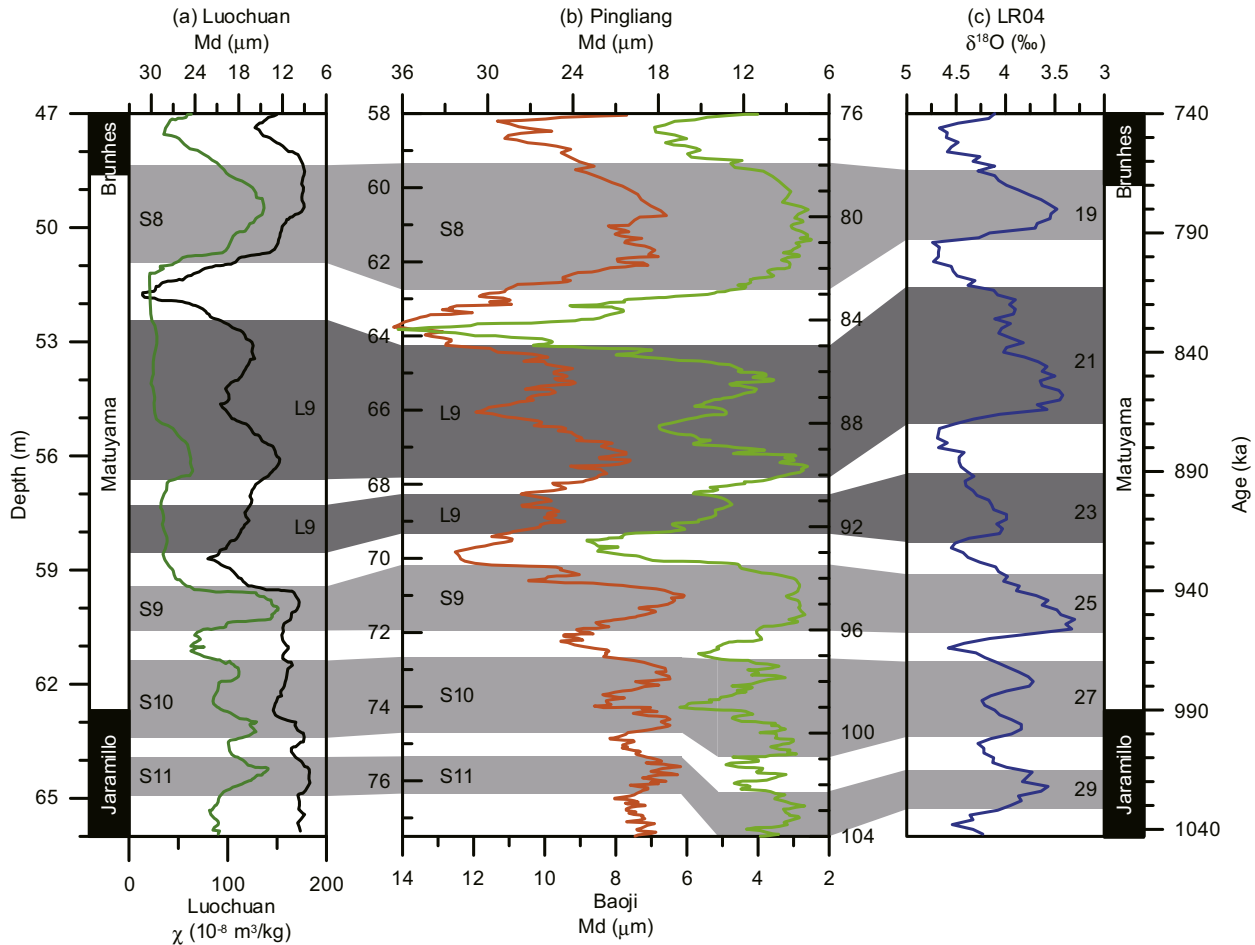
Fig. 11. Correlations between Chinese loess and a stack of 57 globally distributed benthic δ¹⁸O records (Lisiecki and Raymo, 2005). Grass green (dark) line is susceptibility (median grain size, Md) for the Luochan section (Sun and Liu, 2000b) (a). Orange and green lines are Md curves for the Baoji and Pingliang sections, respectively (Ding et al., 2002) (b). S8 and S10 are tied to marine oxygen isotope stages 19 and 27, respectively, according to the correspondence of the Matuyama–Brunhes boundary and the upper-Jaramillo boundary between both loess and marine sediments. (For interpretation of the references to color in this figure legend, the reader is referred to the web version of this article.)

5.2. The remagnetization mechanism for L9

Overall, the NRM of the Chinese loess records includes the DRM carried by magnetite of eolian origin (Zhu et al., 1994a; Yang et al., 2008, 2010), chemical remanent magnetization (CRM) and VRM produced by the newly formed SD/PSD maghemite grains and/or SD/PSD like low-temperature oxidized magnetic particles formed during pedeogenesis processes (Heller and Liu, 1984; Guo et al., 2001; Pan et al., 2001; Liu et al., 2002, 2003b). L9 has experienced the weakest weathering and pedogenesis during the Quaternary (Liu, 1985; Guo et al., 1998). Therefore, the VRM and CRM carried by the pedogenically-produced fine-grained magnetic particles are not sufficient enough to overprint the pDRM and/or the original DRM recorded in L9 as suggested in the Sanmenxia region by Wang et al. (2005).

Wang et al. (2005) attributed the magnetic anomalies in L9 at Sanmenxia section to remagnetization which is caused by physical realignment of magnetic grains. They suggested that the magnetic particles in L9 were physically chaotic by infiltrating rainfall during the interglacial period corresponding to S8, and were finally reoriented along the ambient field in the Brunhes (Wang et al., 2005). However, this mechanism is not applicable in the Luochan area. The MB reversal occurred during the transitional period from S8 to L8 (Jin and Liu, 2010). It is inconceivable that the limited paleoprecipitation during the L8 period in the Brunhes can infiltrate into

the entire L9 through a ∼2 m thick S8 unit, a well developed paleosol unit that is considered as an efficient confining bed (Liu, 1985). In addition, the AMS results display a primary sediment fabric without distinct disturbance except the top 45 cm. Influence of rainfall infiltration on physical realignment of magnetic grains may be limited to only decimeter scales (∼45 cm in the Luochuan area). Regardless, the magnetic particles that carry the ChRM in the deposited dust can be fixed permanently in the direct of the ambient field after initial wetting (Wang and Løvlie, 2010). Therefore, remagnetization caused by physical realignment of magnetic grains for almost the whole L9 can be excluded in the Luochuan area.

Rock magnetism, thermal demagnetization, and SEM results indicate that ChRMs for samples from L9 are dominantly carried by coarse-grained (large PSD and/or MD) magnetite particles of detrital origin. During and after dust deposition on the loess plateau, the loess acquired a DRM, or a pDRM during the post-depositional processes (Liu et al., 2003b). Several studies have shown that coarse-grained magnetite particles are very sensitive to the viscous magnetization (Dunlop, 1983; Tivey and Johnson, 1984; Muxworthy and Williams, 2006a, 2006b; Williams and Muxworthy, 2006). Overprinting of VRM on the coarse-grained eolian magnetite particles, which is of low coercivity, can totally replace its original DRM (Liu et al., 2003b; Deng, 2008). A good correlation between the remagnetization zones (the magnetic

anomalies 1, 3, and 5) and the grain size curve (Md) strongly supports this mechanism (Fig. 8b–f).

In addition, there also exist two magnetically chaotic zones (the magnetic anomalies 2 and 4), in which numerous samples have reversed polarity or virtual geomagnetic pole latitude less than 45°. There is also a magnetically chaotic zone at 74–121 cm that is recognized as the MB transitional zone (Fig. 8d–f). Such behavior has been attributed to the low efficiency of magnetic alignment of the detrital magnetite particles deposited during the MB reversal, which is characterized by a low paleointensity (Jin and Liu, 2010). The magnetic particles in L9 are also largely coarser than that in L8 and S8. SEM results combined with Md indicate a finer-grained nature of magnetite particles in the intervals corresponding to magnetic anomalies 2 and 4, when compared with anomalies 1, 3, and 5. These finer-grained magnetic particles may experience low-grade overprinting of VRM. However, the magnetically chaotic behavior of anomalies 2 and 4 is caused by a combination of low efficiency alignment of magnetic particles, which is dominant factor, and minor VRM overprinting of coarse magnetite particles to some extent. Wang et al. (2005) noted that there are a few samples in the lower part of L9 with a unstable remanence, reflecting randomization of the magnetic particles. This phenomenon further supports the mechanism of low efficiency magnetic alignment proposed in this study. Because of this reason, anomaly 4 should cover the Kamikatsura event, but this cannot be easily distinguished.

6. Conclusions

Multiproxy records of paleoclimatology and environmental magnetism, associated with pedostratigraphy reveal distinct weakening of the winter monsoon corresponding to the intervals of 470–600 and 755–880 cm. An extended climatic optimum over 470–880 cm is proposed to correlated with MIS 21, representing a moderate interglacial. This correlation partly supports Wang et al.'s (2005) scheme. Based on the new correlation between loess and marine $\delta^{18}O$ records from climatostratigraphy and magnetostratigraphy, L9 should be correlated to marine oxygen isotope stages 20–24, which allows a new age model for L9 to be constructed.

Multiproxy records of magnetic mineralogy (especially LT technique) and SEM reveals that the coarse-grained magnetite particles (MD and/or large PSD) are the dominant magnetic carriers. Five magnetic anomalies with different morphologies have been observed in L9 at Luochuan section. Excluding the CRM overprinting and physical realignment of magnetite particles, two alternative mechanisms, such as VRM overprinting and low efficiency magnetic alignment, are suggested to interpret these phenomena. For the magnetic anomalies 1, 3, and 5, a VRM overprinting mechanism was proposed owing to coarse-grained magnetite particles, which were totally overprinted by the VRM acquired during the Brunhes. For the magnetic anomalies 2 and 4, the magnetically chaotic behavior is mainly caused by low efficiency alignment of the magnetic particles along a field with relative low intensity compared with that during the Brunhes. These anomalies are also associated with partial VRM overprinting of coarse magnetite particles. Although the Kamikatsura excursion should be covered by anomaly 4, it cannot be faithfully distinguished due to noisy paleomagnetic recordings. The Santa Rosa excursion is definitely not recorded by L9, and should be recorded by the underlying layers.

In summary, the paleomagnetic and paleoclimatic patterns for L9 are more complex than previously expected. Caution should be taken when interpreting paleomagnetic records of Chinese loess, especially when there is a lack of supports of detailed magnetic mineralogy information and reasonable age controls.

References

An, Z.S., Geogre, J.K., Porter, S.C., Xiao, J.L., 1991. Magnetic susceptibility evidence of monsoon variation in the loess plateau of central China during the last 130,000 years. Quat. Res. 36, 29–36.

An, Z.S., Kutzbach, J.E., Prell, W.L., Porter, S.C., 2001. Evolution of Asian monsoons and phased uplift of the Himalaya-Tibetan plateau since Late Miocene times. Nature 411, 62–66.

Bloemendal, J., Liu, X.M., 2005. Rock magnetism and geochemistry of two plio-pleistocene Chinese loess-palaeosol sequences—implications for quantitative palaeoprecipitation reconstruction. Palaeogeogr. Palaeocl. 225, 149–166.

Channell, J.E.T., Kleiven, H.F., 2000. Geomagnetic palaeointensities and astrochronological ages for the Matuyama–Brunhes boundary and the boundaries of the Jaramillo Subchron: palaeomagnetic and oxygen isotope records from ODP Site 983. Phil. Trans. R. Soc. Lond. A 358, 1027–1047.

Channell, J.E.T., Mazaud, A., Sullivan, P., Turner, S., Raymo, M.E., 2002. Geomagnetic excursions and paleointensities in the Matuyama Chron at Ocean Drilling Program Sites 983 and 984 (Iceland Basin). J. Geophys. Res. 107. doi:10.1029/2001JB000491.

Channell, J.E.T., Raymo, M.E., 2003. Paleomagnetic record at ODP Site 980 (Feni Drift, Rockall) for the past 1.2 Myrs. Geochem. Geophys. Geosyst. 4, 1033. doi:10.1029/2002GC000440.

Chen, F.H., Li, J.J., Zhang, W.X., 1991. Loess stratigraphy of the Lanzhou profile and its comparison with deep-sea sediment and ice core record. GeoJournal 24, 201–209.

Deng, C.L., 2008. Paleomagnetic and mineral magnetic investigation of the Baicaoyuan loess-paleosol sequence of the western Chinese Loess Plateau over the last glacial–interglacial cycle and its geological implications. Geochem. Geophys. Geosyst. 9, Q04034. doi:10.1029/02007GC001928.

Deng, C.L., Shaw, J., Liu, Q.S., Pan, Y.X., Zhu, R.X., 2006. Mineral magnetic variation of the Jingbian loess/paleosol sequence in the northern Loess Plateau of China: implications for Quaternary development of Asian aridification and cooling. Earth Planet. Sci. Lett. 241, 248–259.

Deng, C.L., Vidic, N.J., Verosub, K.L., Singer, M.J., Liu, Q.S., Shaw, J., Zhu, R.X., 2005. Mineral magnetic variation of the Jiaodao Chinese loess//paleosol sequence and its bearing on long-term climatic variability. J. Geophys. Res. 110, B03103. doi:10.1029/02004JB003451.

Deng, C.L., Zhu, R.X., Verosub, K.L., Singer, M.J., Vidic, N.J., 2004. Mineral magnetic properties of loess//paleosol couplets of the central loess plateau of China over the last 1.2 Myr. J. Geophys. Res. 109, B01103. doi:10.1029/02003JB002532.

Deng, C.L., Zhu, R.X., Verosub, K.L., Singer, M.J., Yuan, B.Y., 2000. Paleoclimatic significance of the temperature-dependent susceptibility of Holocene loess along a NW–SE transect in the Chinese loess plateau. Geophys. Res. Lett. 27, 3715–3718.

Derbyshire, E., Keen, D.H., Kemp, R.A., Rolph, T.C., Shaw, J., Meng, X.M., 1995. Loess-palaeosol sequences as recorders of palaeoclimatic variations during the last glacial–interglacial cycle: some problems of correlation in north-central China. In: Derbyshire, E. (Ed.), Wind Blown Sediments in the Quaternary Record, Quaternary Proceedings. Wiley, Chichester, UK, pp. 7–18.

Ding, Z.L., Derbyshire, E., Yang, S.L., Yu, Z.W., Xiong, S.F., 2002. Stacked 2.6-Ma grain size record from the Chinese loess based on five sections and correlation with the deep-sea $\delta^{18}O$ record. Paleoceanography 17, 1033. doi:10.1029/2001PA000725.

Ding, Z.L., Liu, T.S., Rutter, N.W., Yu, Z.W., Guo, Z.T., 1995. Ice-volume forcing of east Asian winter monsoon variations in the past 800,000 years. Quat. Res. 44, 149–159.

Doell, R.R., Dalrymple, G.B., 1966. Geomagnetic polarity epochs: a new polarity event and the age of the brunhes–matuyama boundary. Science 152, 1060–1061.

Dunlop, D.J., 1983. Viscous magnetization of 0.04–100 μm magnetites. Geophys. J. Roy. Astron. Soc. 74, 667–687.

Dunlop, D.J., Özdemir, Ö., 1997. Rock Magnetism: Fundamentals and Frontiers. Cambridge University Press, New York.

Evans, M.E., Heller, F., 2003. Environmental Magnetism: Principles and Applications of Enviromagnetics. Academic Press.

Fang, X.M., Li, J.J., derVoo, R.V., Niocaill, C.M., Dai, X.R., Kemp, R.A., Derbyshire, E., Cao, J.X., Wang, J.M., Wang, G., 1997. A record of the Blake Event during the last interglacial paleosol in the western Loess Plateau of China. Earth Planet. Sci. Lett. 146, 73–82.

Fisher, R.A., 1953. Dispersion on a sphere. Proc. Roy. Soc. Lond. Ser. A 217, 295–305.

Forster, T., Heller, F., 1994. Loess deposits from the Tajik depression (Central Asia): magnetic properties and paleoclimate. Earth Planet. Sci. Lett. 128, 501–512.

Guo, B., Zhu, R.X., Florindo, F., Ding, Z.L., Sun, J.M., 2002a. A short, reverse polarity interval within the Jaramillo subchron: evidence from the Jingbian section, northern Chinese Loess Plateau. J. Geophys. Res. 107. doi:10.1029/2001JB000706.

Guo, B., Zhu, R.X., Florindo, F., Pan, Y.X., Yue, L.P., 2001. Pedogenesis affecting the Matuyama–Brunhes polarity transition recorded in Chinese loess. Chin. Sci. Bull. 46, 975–981.

Guo, Z.T., Berger, A., Yin, Q.Z., Qin, L., 2009. Strong asymmetry of hemispheric climates during MIS-13 inferred from correlating China loess and Antarctica ice records. Climate Past 5.

Guo, Z.T., Liu, T.S., Fedoroff, N., Wei, L.Y., Ding, Z.L., Wu, N.Q., Lu, H.Y., Jiang, W.Y., An, Z.S., 1998. Climate extremes in Loess of China coupled with the strength of deep-water formation in the North Atlantic. Global Planet. Change 18, 113–128.

Guo, Z.T., Ruddiman, W.F., Hao, Q.Z., Wu, H.B., Qiao, Y.S., Zhu, R.X., Peng, S.Z., Wei, J.J., Yuan, B.Y., Liu, T.S., 2002b. Onset of Asian desertification by 22 Myr ago inferred from loess deposits in China. Nature 416, 159–163.

Hao, Q.Z., Guo, Z.T., 2005. Spatial variations of magnetic susceptibility of Chinese loess for the last 600 kyr: implications for monsoon evolution. J. Geophys. Res. 110. doi:10.1029/2005JB003765.

Hao, Q.Z., Oldfield, F., Bloemendal, J., Guo, Z.T., 2008. Particle size separation and evidence for pedogenesis in samples from the Chinese Loess Plateau spanning the past 22 m.y. Geology 36, 727–730.

Heller, F., Beat, M.L., Wang, J.D., Li, H.M., Liu, T.S., 1987. Magnetization and sedimentation history of loess in the central loess plateau of China. In: Liu, T.S. (Ed.), Aspects of Loess Research. China Ocean Press, Beijing.

Heller, F., Evans, M.E., 1995. Loess magnetism. Rev. Geophys. 33, 211–240.

Heller, F., Liu, T.S., 1982. Magnetostratigraphical dating of loess deposits in China. Nature 300, 431–433.

Heller, F., Liu, T.S., 1984. Magnetism of Chinese loess deposits. Geophys. J. Roy. Astron. Soc. 77, 125–141.

Heslop, D., Langereis, C.G., Dekkers, M.J., 2000. A new astronomical timescale for the loess deposits of Northern China. Earth Planet. Sci. Lett. 184, 125–139.

Hunt, C.P., Banerjee, S.K., Han, J.M., Solheid, P.A., Oches, E., Sun, W.W., Liu, T., 1995. Rock-magnetic proxies of climate change in the loess-palaeosol sequences of the western Loess Plateau of China. Geophys. J. Int. 123, 232–244.

Jin, C.S., Liu, Q.S., 2010. Reliability of the natural remanent magnetization recorded in Chinese loess. J. Geophys. Res. 115, B04103. doi:10.1029/02009JB006703.

Kirschvink, J.L., 1980. The least-squares line and plane and the analysis of palaeomagnetic data. Geophys. J. Roy. Astron. Soc. 62, 699–718.

Kukla, G., 1987. Loess stratigraphy in central China. Quat. Sci. Rev. 6, 191–219.

Kukla, G., An, Z.S., 1989. Loess stratigraphy in central China. Palaeogeogr. Palaeocl. 72, 203–225.

Lisiecki, L.E., Raymo, M.E., 2005. A Pliocene–Pleistocene stack of 57 globally distributed benthic $\delta^{18}O$ records. Paleoceanography 20. doi:10.1029/2004PA001071.

Liu, Q.S., Banerjee, S.K., Jackson, M.J., 2003a. An integrated study of the grain-size-dependent magnetic mineralogy of the Chinese loess/paleosol and its environmental significance. J. Geophys. Res. 108, 2437. doi:10.1029/2002JB002264.

Liu, Q.S., Banerjee, S.K., Jackson, M.J., Chen, F.H., Pan, Y.X., Zhu, R.X., 2004a. Determining the climatic boundary between the Chinese loess and palaeosol: evidence from aeolian coarse-grained magnetite. Geophys. J. Int. 156, 267–274.

Liu, Q.S., Banerjee, S.K., Jackson, M.J., Deng, C.L., Pan, Y.X., Zhu, R.X., 2004b. New insights into partial oxidation model of magnetites and thermal alteration of magnetic mineralogy of the Chinese loess in air. Geophys. J. Int. 158, 506–514.

Liu, Q.S., Banerjee, S.K., Jackson, M.J., Deng, C.L., Pan, Y.X., Zhu, R.X., 2005a. Inter-profile correlation of the Chinese loess/paleosol sequences during Marine Oxygen Isotope Stage 5 and indications of pedogenesis. Quat. Sci. Rev. 24, 195–210.

Liu, Q.S., Banerjee, S.K., Jackson, M.J., Zhu, R.X., Pan, Y.X., 2002. Effects of low-temperature oxidation on natural remanent magnetization of Chinese loess. Chin. Sci. Bull. 47, 2100–2105.

Liu, Q.S., Deng, C.L., Yu, Y., Yorrent, J., Jackson, M.J., Banerjee, S.K., Zhu, R.X., 2005b. Temperature dependence of magnetic susceptibility in an argon environment: implications for pedogenesis of Chinese loess/palaeosols. Geophys. J. Int. 161, 102–112.

Liu, Q.S., Jackson, M.J., Banerjee, S.K., Zhu, R.X., Pan, Y.X., Chen, F.H., 2003b. Determination of magnetic carriers of the characteristic remanent magnetization of Chinese loess by low-temperature demagnetization. Earth Planet. Sci. Lett. 216, 175–186.

Liu, Q.S., Roberts, A.P., Torrent, J., Horng, C.-S., Larrasoaña, J.C., 2007. What do the HIRM and S-ratio really measure in environmental magnetism? Geochem. Geophys. Geosyst. 8, Q09011. doi:10.1029/02007GC001717.

Liu, Q.S., Roberts, A.P., Rohling, E.J., Zhu, R.X., Sun, Y.B., 2008. Post-depositional remanent magnetization lock-in and the location of the Matuyama–Brunhes geomagnetic reversal boundary in marine and Chinese loess sequences. Earth Planet. Sci. Lett. 275, 102–110.

Liu, T.S., 1985. Loess and the Environment. China Ocean Press, Beijing.

Liu, T.S., Ding, Z.L., 1998. Chinese loess and the paleomonsoon. Annu. Rev. Earth Planet. Sci. 26, 111–145.

Liu, T.S., Ding, Z.L., Rutter, N., 1999. Comparison of Milankovitch periods between continental loess and deep sea records over the last 2.5 Ma. Quat. Sci. Rev. 18, 1205–1212.

Liu, W.M., Zhang, L.Y., Sun, J.M., 2010. High resolution magnetostratigraphy of the Luochuan loess-paleosol sequence in the central Chinese Loess Plateau (in Chinese with English abstract). Chin. J. Geophys. 53, 888–894.

Liu, X.M., Liu, T.S., Xu, T.C., Liu, C., Chen, M.Y., 1988a. The Chinese loess in Xifeng, I. The primary study on magnetostratigraphy of a loess profile in Xifeng area, Gansu province. Geophys. J. 92, 345–348.

Liu, X.M., Xu, T.C., Liu, T.S., 1988b. The Chinese loess in Xifeng, II. A study of anisotropy of magnetic susceptibility of loess from Xifeng. Geophys. J. 92, 349–353.

Maenaka, M., 1983. Magnetostratigraphic study of the Osaka group, with special reference to the existence of pre- and post-jaramillo episodes in the late Matuyama polarity epoch. Mem. Hanazono Univ. 14, 1–65.

Maher, B.A., Thompson, R., 1995. Paleorainfall reconstructions from pedogenic magnetic susceptibility variations in the Chinese loess and paleosols. Quat. Res. 44, 383–391.

Muxworthy, A.R., Williams, W., 2006a. Low-temperature viscous magnetization of multidomain magnetite: evidence for disaccommodation contribution. J. Magn. Magn. Mater. 307, 113–119.

Muxworthy, A.R., Williams, W., 2006b. Observations of viscous magnetization in multidomain magnetite. J. Geophys. Res. 111, B01103. doi:10.1029/02005JB003902.

Pan, Y.X., Zhu, R.X., Liu, Q.S., Guo, B., Yue, L.P., Wu, H.N., 2002. Geomagnetic episodes of the last 1.2 Myr recorded in Chinese loess. Geophys. Res. Lett. 29, 123,121–123,124.

Pan, Y.X., Zhu, R.X., Shaw, J., Liu, Q.S., Guo, B., 2001. Can relative paleointensities be determined from the normalized magnetization of the wind-blown loess of China? J. Geophys. Res. 106, 19221–19232.

Porter, S.C., 2001. Chinese loess record of monsoon climate during the last glacial–interglacial cycle. Earth Sci. Rev. 54, 115–128.

Ruddiman, W.F., Raymo, M.E., Martinson, D.G., Clement, B.M., Backman, J., 1989. Pleistocene evolution: northern hemisphere ice sheets and north Atlantic ocean. Paleoceanography 4, 353–412.

Rutter, N., Ding, Z.L., Evans, M.E., Liu, T.S., 1991. Baoji-type pedostratigraphic section, loess plateau, north-central China. Quat. Sci. Rev. 10, 1–22.

Shackleton, N.J., Berger, A., Peltier, W.R., 1990. An alternative astronomical calibration of the lower Pleistocene timescale based on ODP Site 677. Trans. Roy. Soc. Edinb. Earth Sci. 81, 251–261.

Spassov, S., Heller, F., Evans, M.E., Yue, L.P., Dobeneck, T.v., 2003. A lock-in model for the complex Matuyama–Brunhes boundary record of the loess/palaeosol sequence at Lingtai (Central Chinese Loess Plateau). Geophys. J. Int. 155, 350–366.

Sun, D.H., Shaw, J., An, Z.S., Cheng, M.Y., Yue, L.P., 1998. Magnetostratigraphy and paleoclimatic interpretation of a continuous 7.2 Ma Cenozoic eolian sediments from the Chinese Loess Plateau. Geophys. Res. Lett. 25, 85–88.

Sun, J.M., 2002. Provenance of loess material and formation of loess deposits on the Chinese Loess Plateau. Earth Planet. Sci. Lett. 203, 845–859.

Sun, J.M., 2005. Long-term fluvial archives in the Fen Wei Graben, central China, and their bearing on the tectonic history of the India–Asia collision system during the Quaternary. Quat. Sci. Rev. 24, 1279–1286.

Sun, J.M., Huang, X.G., 2006. Half-precessional cycles recorded in Chinese loess: response to low-latitude insolation forcing during the Last Interglaciation. Quat. Sci. Rev. 25, 1065–1072.

Sun, J.M., Liu, T.S., 2000a. Multiple origins and interpretations of the magnetic susceptibility signal in Chinese wind-blown sediments. Earth Planet. Sci. Lett. 180, 287–296.

Sun, J.M., Liu, T.S., 2000b. Stratigraphic evidence for the uplift of the Tibetan Plateau between 1.1 and 0.9 myr ago. Quat. Res. 54, 309–320.

Sun, J.M., Ye, J., Wu, W.Y., Ni, X.J., Bi, S.D., Zhang, Z.Q., Liu, W.M., Meng, J., 2010a. Late Oligocene–Miocene mid-latitude aridification and wind patterns in the Asian interior. Geology 38, 515–518.

Sun, J.M., Zhu, X.K., 2010. Temporal variations in Pb isotopes and trace element concentrations within Chinese eolian deposits during the past 8 Ma: implications for provenance change. Earth Planet. Sci. Lett. 290, 438–447.

Sun, Y.B., Clemens, S.C., An, Z.S., Yu, Z.W., 2006. Astronomical timescale and palaeoclimatic implication of stacked 3.6-Myr monsoon records from the Chinese Loess Plateau. Quat. Sci. Rev. 25, 33–48.

Sun, Y.B., Wang, X.L., Liu, Q.S., Clemens, S.C., 2010b. Impacts of post-depositional processes on rapid monsoon signals recorded by the last glacial loess deposits of northern China. Earth Planet. Sci. Lett. 289, 171–179.

Tauxe, L., Herbert, T., Shackleton, N.J., Kok, Y.S., 1996. Astronomical calibration of the Matuyama–Brunhes boundary: consequences for magnetic remanence acquisition in marine carbonates and the Asian loess sequences. Earth Planet. Sci. Lett. 140, 133–146.

Tivey, M., Johnson, H.P., 1984. The characterization of viscous remanent magnetization in large and small magnetite particles. J. Geophys. Res. 89, 543–552.

Tsoar, H., Pye, K., 1987. Dust transport and the question of desert loess formation. Sedimentology 34, 139–153.

van Velzen, A.J., Dekkers, M.J., 1999. Low-temperature oxidation of magnetite in loess-paleosol sequences: a correction of rock magnetic parameters. Studia geoph et geod 43, 357–375.

Wang, D.J., Wang, Y.C., Han, J.T., Duan, M.G., Shan, J.Z., Liu, T.S., 2010. Geomagnetic anomalies recorded in L9 of the Songjiadian loess section in southeastern Chinese Loess Plateau. Chin. Sci. Bull. 55, 520–529.

Wang, R.H., Løvlie, R., 2010. Subaerial and subaqueous deposition of loess: experimental assessment of detrital remanent magnetization in Chinese loess. Earth Planet. Sci. Lett. doi:10.1016/j.epsl.2010.1008.1019.

Wang, X.S., Løvlie, R., Yang, Z.Y., Pei, J.L., Zhao, Z.Z., Sun, Z.M., 2005. Remagnetization of Quaternary eolian deposits: a case study from SE Chinese Loess Plateau. Geochem. Geophys. Geosyst. 6, Q06H18. doi:10.1029/2004GC000901.

Wang, X.S., Yang, Z.Y., Løvlie, R., Sun, Z.M., Pei, J.L., 2006. A magnetostratigraphic reassessment of correlation between Chinese loess and marine oxygen isotope records over the last 1.1 Ma. Phys. Earth Planet. Inter. 159, 109–117.

Williams, W., Muxworthy, A.R., 2006. Understanding viscous magnetization of multidomain magnetite. J. Geophys. Res. 111, B02102. doi:10.1029/02005JB003695.

Xiong, S.F., Ding, Z.L., Liu, T.S., 2001. Climatic implications of loess deposits from the Beijing region. J. Quat. Sci. 16, 575–582.

Yang, S.L., Ding, Z.L., 2010. Drastic climatic shift at 2.8 Ma as recorded in eolian deposits of China and its implications for redefining the Pliocene–Pleistocene boundary. Quat. Int. 219, 37–44.

Yang, T.S., Hyodo, M., Yang, Z.Y., Ding, L., Li, H.D., Fu, J.L., Wang, S.B., Wang, H.W., Mishima, T., 2008. Latest Olduvai short-lived reversal episodes recorded in Chinese loess. J. Geophys. Res. 113, B05103. doi:10.1029/02007JB005264.

Yang, T.S., Hyodo, M., Yang, Z.Y., Fu, J.L., 2004. Evidence for the Kamikatsura and Santa Rosa excursions recorded in eolian deposits from the southern Chinese Loess Plateau. J. Geophys. Res. 109, B12105. doi:10.1029/12004JB002966.

Yang, T.S., Hyodo, M., Yang, Z.Y., Fu, J.L., 2007. Two geomagnetic excursions during the Brunhes chron recorded in Chinese loess-palaeosol sediments. Geophys. J. Int. 171, 104–114.

Yang, T.S., Hyodo, M., Yang, Z.Y., Li, H.D., Maeda, M., 2010. Multiple rapid polarity swings during the Matuyama–Brunhes (M-B) transition from two high-resolution loess-paleosol records. J. Geophys. Res. 115, B05101. doi:10.1029/02009JB006301.

Yue, L.P., 1989. Magnetostratigraphical study of the loess section at Duanjiapo, Lantian, Shaanxi (in Chinese with an English abstract). Geol. Rev. 35, 479–488.

Yue, L.P., 1995. Palaeomagnetic polarity boundary were recorded in Chinese loess and red clay, and geological significance. Acta Geophys. Sinica 38, 311–320.

Yue, L.P., Qu, H.J., Yang, Y.L., Ge, T.M., Wen, S.Y., 1992. Paleomagnetic research of loess section from Jiuzhoutai, Lanzhou (in Chinese with an English abstract). J. Northwest Univ. 22, 87–94.

Zeng, Y.N., Ma, H.Z., Li, Z., Li, L.Q., 1993. Palaeomagnetic study on the Dadunling loess profile in Xining (in Chinese with an English abstract). Arid Land Geogr. 16, 77–81.

Zhao, X., Roberts, A.P., 2010. How does Chinese loess become magnetized? Earth Planet. Sci. Lett. 292, 112–122.

Zhao, Z.Z., Jiang, F.C., Wu, X.H., Wang, S.B., Qiao, Y.S., Liu, K., Wang, S.M., 2006. Sanmenxia loess and paleoenvironmental change. J. China Univ. Geosci. 17, 283–290.

Zheng, H.B., An, Z.S., Shaw, J., 1992. New contributions to Chinese Plio–Pleistocene magnetostratigraphy. Phys. Earth Planet. Inter. 70, 146–153.

Zheng, H.B., Huang, X.T., Ji, J.L., Liu, R., Zeng, Q.Y., Jiang, F.C., 2007. Ultra-high rates of loess sedimentation at Zhengzhou since State 7: implication for the Yellow River erosion of the Sanmen Gorge. Geomorphology 85, 131–142.

Zheng, H.B., Rolph, T., Shaw, J., An, Z.S., 1995. A detailed palaeomagnetic record for the last interglacial period. Earth Planet. Sci. Lett. 133, 339–351.

Zhou, L.P., Shackleton, N.J., 1999. Misleading positions of geomagnetic reversal boundaries in Eurasian loess and implications for correlation between continental and marine sedimentary sequences. Earth Planet. Sci. Lett. 168, 117–130.

Zhu, R.X., Laj, C., Mazaud, A., 1994a. The Matuyama–Brunhes and Upper Jaramillo transitions recorded in a loess section at Weinan, north-central China. Earth Planet. Sci. Lett. 125, 143–158.

Zhu, R.X., Liu, Q.S., Jackson, M.J., 2004. Paleoenvironmental significance of the magnetic fabrics in Chinese loess-paleosols since the last interglacial (<130 ka). Earth Planet. Sci. Lett. 221, 55–69.

Zhu, R.X., Liu, Q.S., Pan, Y.X., Deng, C.L., Zhang, R., Wang, X.F., 2006. No apparent lock-in depth of the Laschamp geomagnetic excursion: evidence from the Malan loess. Sci. China Ser. D Earth Sci. 49, 960–967.

Zhu, R.X., Pan, Y.X., Guo, B., Liu, Q.S., 1998. A recording phase lag between ocean and continent climate changes: constrained by the Matuyama/Brunhes polarity boundary. Chin. Sci. Bull. 43, 1593–1598.

Zhu, R.X., Pan, Y.X., Liu, Q.S., 1999. Geomagnetic excursions recorded in Chinese loess in the last 70,000 years. Geophys. Res. Lett. 26, 505–508.

Zhu, R.X., Zhang, R., Deng, C.L., Pan, Y.X., Liu, Q.S., Sun, Y.B., 2007. Are Chinese loess deposits essentially continuous? Geophys. Res. Lett. 34, L17306. doi:10.1029/12007GL030591.

Zhu, R.X., Zhou, L.P., Laj, C., Mazaud, A., Ding, Z.L., 1994b. The Blake geomagnetic polarity episode recorded in Chinese loess. Geophys. Res. Lett. 21, 697–700.